AIMS Energy, 14(5): 1276–1298.
DOI: 10.3934/energy.2026050
Received: 27 July 2026
Revised: 26 September 2026
Accepted: 20 October 2026
Published: 28 October 2026

https://www.aimspress.com/journal/energy

Research article

Research and parameter optimization of SAH enhanced heat transfer characteristics based on sinusoidal corrugated heat absorb plate

Liang Wang[1,4,*], Wenke Zhang[2], Xiaole Wang[2] and Binguang Jia[3]

[1] Shandong Huayu University of Technology, College of Energy and Building Engineering, Dezhou, 253034, China
[2] School of Thermal Engineering, Shandong Jianzhu University, Jinan, Shandong 250101, China
[3] School of Energy and Machinery, Dezhou University, Dezhou, 253023, China
[4] Shandong Engineering Research Center of Low-Carbon Energy Internet of Things Technology, Dezhou, 253034, China

* **Correspondence:** Email: wanglianglre@163.com; Tel: +86 15662717936.

Abstract: The thermal performance of solar air heater (SAH) is the standard for evaluating SAH. To enhance the thermal performance of SAH, we proposed the novel configuration incorporating the sinusoidal corrugated absorb plate. The thermal characteristics of sinusoidal-corrugated SAH were systematically investigated using the combined approach of numerical simulation and theoretical analysis. First, comparative study with conventional triangular-corrugated SAH was conducted, demonstrating the superior comprehensive performance of the sinusoidal plate in enhancing heat transfer while mitigating flow resistance. Second, the effects of key geometric parameters of the sinusoidal corrugation (wavelength and wave height) on the collector efficiency and pressure drop were thoroughly analyzed, leading to the identification of optimized parameter range. Furthermore, the double-layer sinusoidal-corrugated SAH model was developed to explore its synergistic heat transfer enhancement mechanism. The results indicated that the sinusoidal corrugation effectively disrupted the thermal boundary layer and induced secondary flows, which has higher heat collection efficiency and lower pressure drop and heat dissipation coefficient. The optimal wavelength was 20 mm, and the optimal wave height was 15 mm, the maximum heat collection efficiency was 61.58%, and the minimum heat dissipation coefficient was 4.66 W/m·K. The double-layer structure further enhanced the heat output. Based on simulated data, the high-precision fitting relationship ($R^2 > 0.98$) was established between the heat collection efficiency and inlet air Reynolds number (*Re*). This study provides theoretical basis and data support for the design and optimization of high-efficiency SAH.

Keywords: SAH; sinusoidal corrugated plate; heat transfer enhancement; parameter optimization; heat collection performance

Abbreviations: SAH: solar air heater; PEC: performance evaluation criterion; Re: Reynolds number; PC: polycarbonate; PCM: phase change material

1. Introduction

In the field of solar thermal utilization, solar air heater (SAH) has garnered extensive research and application due to its advantages such as simple structure, lower cost, no need for frost protection, and direct applicability in space heating, crop drying, and industrial process heating [1]. The application of SAHs in smart buildings, thermal management, and air quality control is receiving increasing attention, particularly in enhancing the sustainability of the built environment [2,3]. However, traditional flat-plate SAHs suffer from low convective heat transfer coefficients between the absorber plate and the air owing to the low thermal capacity and thermal conductivity of air. Consequently, research on SAHs has primarily focused on improving thermal efficiency, reducing energy consumption, and optimizing design [4,5].

To address the issue of low thermal efficiency in SAHs, research has proposed combining stagnation jets with corrugated plates to evaluate Nusselt number and pressure loss [6,7]. V-corrugated plates [8] can effectively increase the heat exchange area and guide airflow, with studies examining SAH thermal performance by integrating designs such as parallel [9] and triple-channel V-corrugations [10]. From the optimization design perspective, research has explored Chevron-type corrugated absorb plates [11] and analyzed absorber plates with different corrugation forms [12]. Other approaches include adding roughness elements on the absorber plate to enhance airflow turbulence and vortices [13], as well as studying the performance of SAHs with V-shaped fins [14], arc-shaped fins [15], S-shaped fins [16], conical ring fins [17], and helical baffles [18]. Additionally, some researchers have optimized the overall SAH structure by incorporating perforated obstacles to improve heat transfer through mixing effects and enhanced turbulence [19]. Rajkumar and Rajkumar employed CFD to investigate the influence of roughness element coverage percentage and positioning on hydrodynamic and thermal behavior [20,21]. Prasad introduced offset transverse ribs in SAHs to examine the impact of airflow between the ribs and the absorb plate on heat transfer enhancement [22]. Kanjirakat attached tetrahedron-shaped turbulators to the bottom of the absorb plate, which significantly improved the SAH's heat transfer efficiency [23].

Furthermore, some scholars have conducted research on multi-pass SAHs, aiming to enhance thermal efficiency by extending the airflow path [24] and increasing the heat exchange duration [25,26]. Wang designed a novel SAH that combines the downward impingement jet with corrugated absorber plate, optimizing flow and temperature fields to improve heat transfer efficiency [27]. Li et al. proposed a transversal corrugated target plate with a corrugation tilt angle, which regulates the flow velocity of the crossflow to enhance heat transfer [28]. Studies on the CFD model validation and combined thermal-exergetic performance evaluation of V-corrugated absorber plates reported that as the inlet air flow rate increases from 100 m^3/h to 400 m^3/h, the average hot air temperature at the outlet of the solar air collector decreases from 62.9 °C to 46.6 °C. At the end of the drying process, the moisture ratios of potato, carrot, and apple rise to 116.95%, 126.70%, and 118.77%, respectively [29]. Another investigation

on SAHs integrated with finned hollow cylindrical obstacles and phase change material (PCM) revealed that the time-averaged thermal efficiency of the finned configuration is higher. Its time-averaged exergetic efficiency reaches approximately 3.46%, which is 34.62% higher than that of HCOF and 128.01% higher than that of HCO [30].

Based on research, in comparison with traditional flat plates, sinusoidal corrugations geometric configuration characterized by continuous and smooth curvature variations have been demonstrated in fields such as shell-and-tube heat exchangers to achieve the better balance between enhanced heat transfer and controlled pressure drop. However, the application of sinusoidal corrugated structures to SAH absorb plates remains insufficiently explored, and their comprehensive performance advantages over classical triangular corrugations have yet to be systematically quantified. Furthermore, the influence of key geometric parameters of sinusoidal corrugations, such as wavelength and wave height, on SAH performance remains unclear, lacking systematic parametric optimization studies. Extending from single-pass to the double-pass flow channel represents another effective approach to increasing the thermal output per unit area of SAHs; yet, the synergistic enhancement mechanisms and performance potential of double-pass SAHs incorporating sinusoidal corrugations remain to be elucidated.

In light of this, we aim to systematically investigate the thermal performance of sinusoidal corrugated plate SAHs and to validate their performance advantages through comparative analysis with triangular corrugated plates. In terms of the novelty of this study, the main contributions compared with previous investigations are summarized as follows:

1. Thermal performance comparison between sinusoidal and V-corrugated SAHs is conducted. Apart from collector efficiency and pressure drop, the performance evaluation criterion (PEC) is also adopted for comprehensive comparison.
2. Parametric analysis of the sinusoidal corrugated absorber plate is carried out. The importance of PEC for SAH thermal performance assessment is emphasized, and the optimal coupled structural parameters are identified.
3. The double-pass SAH model is established to demonstrate its thermal performance advantages over the single-pass configuration. Comparisons between parallel-flow and counter-flow air arrangements are also supplemented.
4. Curve fitting is performed to characterize the coupling relationship between thermal efficiency and *Re* for the double-pass SAH. The generalizability of the fitted correlation is discussed, which provides theoretical support for future experimental investigations.

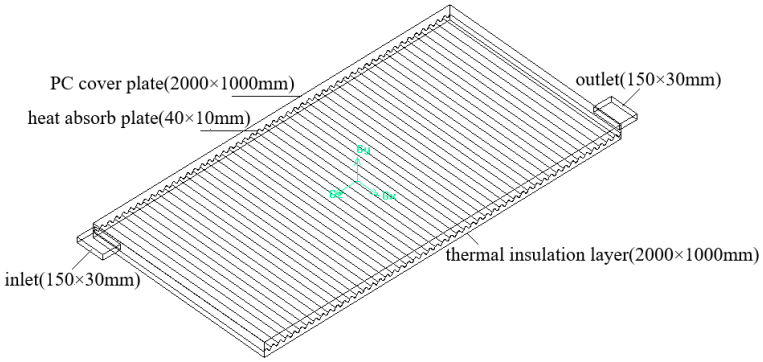
Here, we elucidate the heat transfer mechanism of sinusoidal-corrugated plate SAH and seeks to address the research gap regarding the mechanistic improvement of their thermal performance.

2. SAHs physical model validation and boundary condition

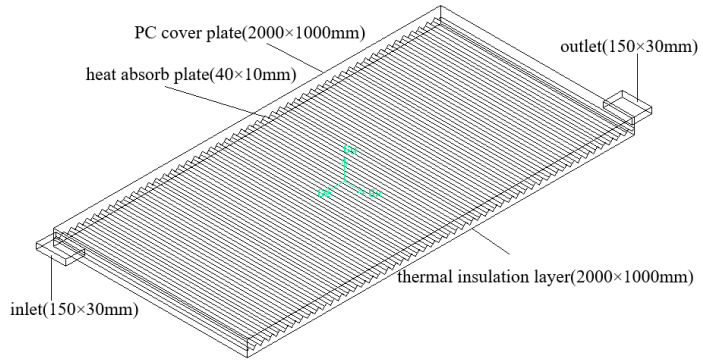
2.1. SAHs physical model

The physical models of sinusoidal corrugated plate SAH and triangular corrugated plate SAH are shown in Figure 1. Figure 1(a) indicates the sinusoidal corrugated plate SAH, while Figure 1(b) inflects the triangular corrugated plate SAH. SAH consists of a polycarbonate (PC) cover plate, corrugated heat absorb plate, insulation layer, and outer shell. The material of the cover plate is PC, with size of 2000 × 1000 mm and thickness is 4 mm. The material of the heat absorb plate is aluminum, with aluminum nitrogen aluminum coating on the surface, and a size of 2000 × 1000 mm and a thickness

of 3 mm. The material of insulation layer is asbestos rock, with a size of 2000 × 1000 mm and a thickness of 30 mm. The air inlet and outlet dimensions are 150 × 30 mm, and the air flow channel height is 50 mm. Air enters the flow channel through the SAH inlet and undergoes heat exchange with the corrugated heat absorb plate. After heat exchange, air flows out of SAH through the outlet.



(a) sinusoidal plate SAH.



(b) triangular plate SAH.

Figure 1. Physical models of two types SAH.

2.2. Governing equations

The equations involved in the heat transfer process include continuity equation, momentum equation, and energy equation [31]. The continuity equation in the flow channel is as follows [31]:

$$\frac{\partial \rho}{\partial \tau}+\frac{\partial（\rho u）}{\partial x}+\frac{\partial（\rho v）}{\partial y}+\frac{\partial（\rho w）}{\partial z}=0 \tag{1}$$

ρ is the density, kg/m^3; τ is the time, s; and u,v,w are the velocity component, m/s.

The momentum equation in the flow channel is as follows [31]:

$$\rho\frac{DV}{D\tau}=F-\nabla p+\mu\nabla^2 V \tag{2}$$

V is specific volume, m^3/kg; τ is time, s; F is volume force, N; p is pressure, pa; and μ is dynamic viscosity, pa·s.

The energy equation in the flow channel is as follows [32]:

$$\frac{\partial T}{\partial \tau}+(u\frac{\partial T}{\partial x}+v\frac{\partial T}{\partial y}+w\frac{\partial T}{\partial z})=\frac{\lambda}{\rho c}\cdot(\frac{\partial^2 T}{\partial x^2}+\frac{\partial^2 T}{\partial y^2}+\frac{\partial^2 T}{\partial z^2})+S \tag{3}$$

T is temperature, K; λ is thermal conductivity, W/m·K; c is specific heat capacity, J/kg·K; and S is source.

The turbulence model is used in the calculations. Turbulence fluctuations occur when air flows over the corrugated SAH plate, resulting in localized vortices. The laminar flow model cannot capture the mixing effects of turbulence and would significantly underestimate the Nu and localized vortices. Therefore, the turbulence model is selected. For the steady-state flow process of fluid with constant physical properties, the governing equations also include the K equation and the ε equation. The K equation in the channel is as follows [33]:

$$\frac{\partial}{\partial t}(\rho K)+\frac{\partial}{\partial x_j}(\rho K u_j)=\frac{\partial}{\partial x_j}[(\mu+\frac{\mu_t}{\sigma_k})\frac{\partial K}{\partial x_j}]+P_k+P_b-\rho\varepsilon-Y_k+S_k \tag{4}$$

K is turbulent kinetic energy, J; μ_j is direction of velocity component j; μ_t is unsteady dynamic viscosity, pa·s; σ_k is turbulent Prandtl number, σ_k = 1.0; P_k is turbulent kinetic energy caused by the average velocity gradient, J; P_b is turbulent kinetic energy caused by buoyancy, J; ε is turbulent dissipation rate; Y_k is the influence of compressible turbulent pulsation expansion on dissipation rate; and S_k is turbulent energy source.

The ε equation is as follows [33]:

$$\frac{\partial}{\partial t}(\rho\varepsilon)+\frac{\partial}{\partial x_j}(\rho\varepsilon u_j)=\frac{\partial}{\partial x_j}[(\mu+\frac{\mu_t}{\sigma_\varepsilon})\frac{\partial\varepsilon}{\partial x_j}]+\rho C_{1\varepsilon}S_\varepsilon-\rho C_{2\varepsilon}\frac{\varepsilon^2}{K+\sqrt{v\varepsilon}}+C_{1\varepsilon}\frac{\varepsilon}{K}C_{3\varepsilon}P_b+S_k \tag{5}$$

$C_{1\varepsilon}$ is constant, $C_{1\varepsilon}$ = 1.44; $C_{2\varepsilon}$ is constant, $C_{2\varepsilon}$ = 1.92; $C_{3\varepsilon}$ is constant, $C_{3\varepsilon}$ = 0.09; and S_k is turbulent dissipation rate source.

In the selection of radiation models, the DO radiation model is chosen as the radiation model for this research. The reason is: The DO model can simulate and calculate all steady-state optical radiation. The equation of the DO model is as follows [34]:

$$\frac{dI_\lambda(\boldsymbol{r},\ \boldsymbol{s})}{ds}+(a+\sigma_s)\ dI_\lambda(\boldsymbol{r},\ \boldsymbol{s})=an^2\frac{\sigma T^4}{\pi}+\frac{\sigma_s}{4\pi}\int_0^{4\pi}I_\lambda(\boldsymbol{r},\ \boldsymbol{s})\ \Phi(\boldsymbol{s},\ \boldsymbol{s})\ d\Omega \tag{6}$$

I_λ is solar radiation intensity, W/m^2; s is air channel length, m; $\boldsymbol{r}$ is position vector; $\boldsymbol{s}$ is direction vector; a is spectral absorption coefficient; σ_s is spectral scattering coefficient; n is spectral refractive coefficient; σ is Stephen Boltzmann constant, $\sigma = 5.67\times10^{-8}$ $W/m^2\cdot K^4$; ϕ is scattering phase function; and Ω is light source emission solid angle, °.

2.3. Boundary condition setting

Numerical simulations are performed using Fluent 16.0 with constant thermophysical properties of air. The solar load model built in Fluent is adopted for the calculation. The simulated latitude and longitude of this study are 117° and 36°4′, and the simulation calculation time is 12:00 on March 1st. The solar azimuth vector is $x = -0.690846$, $y = 0.7152947$, and $z = 0.1052865$. The outer surface of the SAH PC cover plate is subjected to natural convection. Inlet turbulence intensity is set to 10%. The pressure–velocity coupling algorithm is adopted, and the second-order upwind scheme is selected for discretization. Inlet turbulent flow rate is 10%. There is also natural convection outside the PC cover plate. The direct solar irradiance is 682 W/m²·K, and the transmittance of the PC cover plate is 0.83. The velocity basis and pressure basis are coupled at the air inlet and outlet, with the air inlet as the velocity inlet boundary condition and the outlet as the pressure outlet boundary condition, and the atmospheric transparency is set to 0.7. The boundary conditions of the SAH components are shown in Table 1.

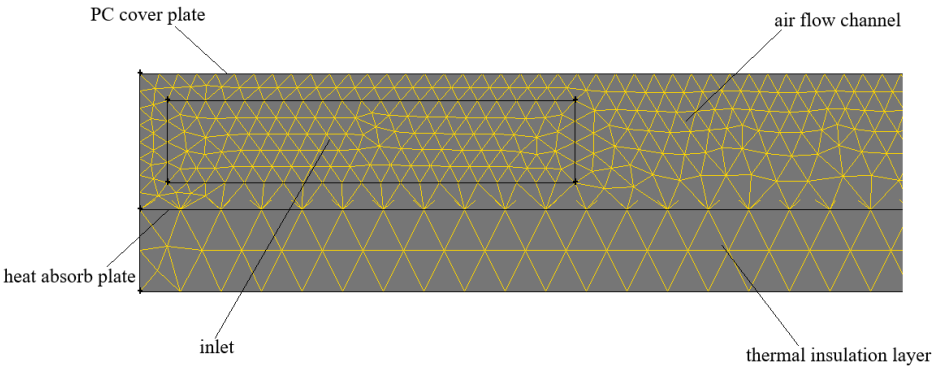
Table 1. Boundary condition setting.

Structure name	Boundary setting
PC cover plate	Mixed boundary of convection and radiation, semitransparent medium, absorption rate 0.09, transmittance 0.83, refractive index 1.5
Heat absorb plate	Fluid structure coupling boundary, opaque medium, absorption rate 0.9, emissivity 0.08
Thermal insulation layer	Adiabatic boundary, opaque medium
Shell	Adiabatic boundary, opaque medium

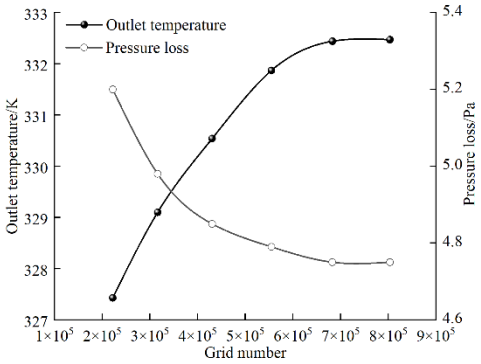
For the research process, we use a three-dimensional dual precision pressure basis to solve the problem. The turbulence model uses the Realizable k-ε model. Compared to the standard k-ε model, the calculation equation for fluid turbulent viscosity is added. Furthermore, according to references [32,33], the Realizable k-ε model can yield predictions closer to the practical operating conditions. The radiation model adopts the DO model. There is also a pressure difference between the air inlet and outlet, so the calculation process uses the SIMPLE algorithm to improve.

2.4. Grid division and model validation

For the above-mentioned sinusoidal corrugated plate SAH model, GAMBIT is used to partition the SAH model mesh. The grid format is unstructured tetrahedral TGrid. The reason is that unstructured grids are suitable for complex models, and compared to structured grids, unstructured grids have computational stability. Moreover, the air inlet and outlet, corrugated heat absorb plate, and air flow channel are encrypted. Additionally, the air flow channel of SAH belongs to the fluid domain, which is the significant calculation part that requires accuracy. The SAH model grid division and independent verification are shown in Figure 2.



(a) Sinusoidal plate SAH model mesh division.



(b) Sinusoidal plate SAH model grid verification.

Figure 2. Sinusoidal plate SAH grid division and verification.

Figure 2 presents the mesh generation and mesh independence verification of the sinusoidal-corrugated SAH model. Figure 2(a) shows the mesh discretization of the model and mesh refinement in the internal fluid domain. The near-wall treatment with wall functions is adopted. The formula for the dimensionless wall distance y^+ of the boundary layer is given as follows:

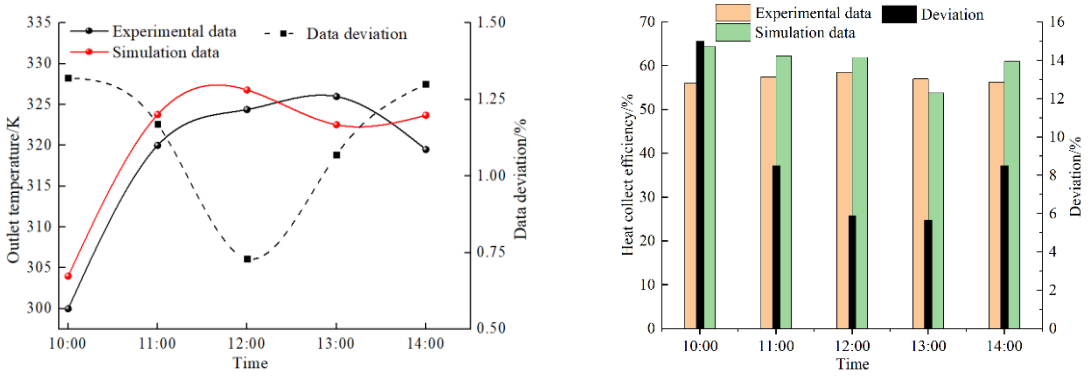
$$y^+ = \frac{y}{\upsilon}\sqrt{\frac{\tau_\omega}{\rho}} \tag{7}$$

y^+ is the dimensionless wall distance of the boundary layer; y denotes the physical distance from the centroid of the first near-wall cell to the wall, m; and τ_ω is Wall shear stress, Pa.

From the calculation, the overall y^+ is 30. Figure 2(b) illustrates the mesh independence test, where the air outlet temperature and pressure drop of the SAH are selected as monitoring indicators. The data in Figure 2(b) reveal that the SAH outlet temperature rises and the pressure drop decreases with the increase in grid number. When the grid number reaches 6.8×10^5, the outlet temperature and pressure drop of the SAH remain nearly unchanged. Therefore, considering the accuracy and precision of numerical simulations, the grid adopted for the SAH model is 6.8×10^5.

Before simulating the model, the simulation calculation method should be validated first. The selected experimental data comes from reference [35]. Based on the experimental model selected in reference [35], the numerical model with the same structural dimensions is established and simulated

under the same conditions. The comparative verification results are shown in Figure 3.



(a) Outlet temperature. (b) Heat collection efficiency.

Figure 3. Comparison of experimental and simulation data.

The calculation /m.n formula for data deviation is as follows:

$$D_{e-s} = \frac{|T_e - T_s|}{T_e} \tag{8}$$

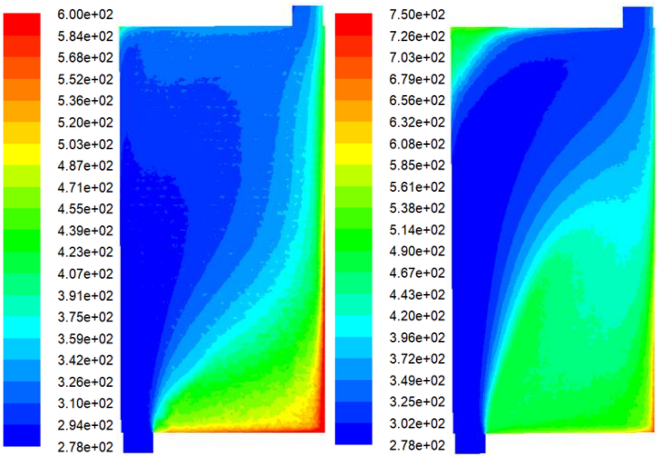
$D_{e\text{-}s}$ is experimental data and simulation data deviation; T_e is experimental temperature value, K; and T_s is simulation temperature value, K.

Figure 3 presents the validation comparison between experimental measurements and numerical simulations, including the air outlet temperature and thermal efficiency. As indicated by the deviations shown in the figure, under identical operating conditions, the deviation of the air outlet temperature is no more than 1.5%, while the maximum deviation of thermal efficiency does not exceed 15% and remains below 10% for most cases. Such deviations are considered acceptable for practical engineering applications. This also verifies the feasibility and correctness of the boundary conditions and numerical methods adopted in the simulation. Accordingly, the above numerical methods and boundary conditions are employed for the simulation and analysis in this research.

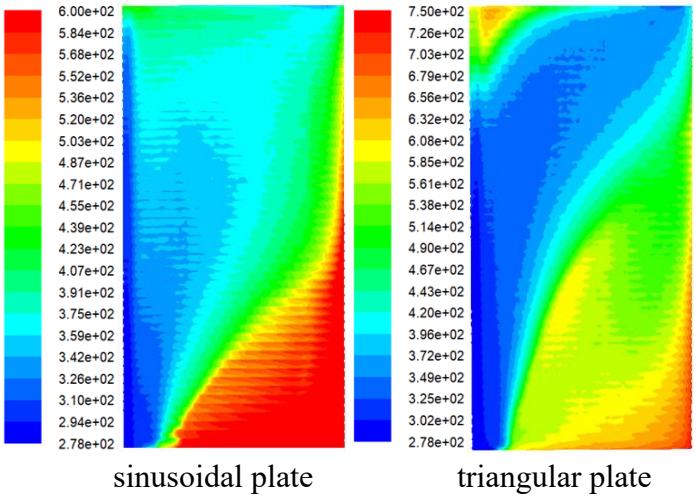
3. Results and discussion

3.1. Analysis and comparison of heat absorb plates with different structures

Initially, based on the different structures of the heat absorb plate, the influence of sinusoidal corrugated plate and triangular corrugated plate structures on the heat collection performance of SAH is compared and studied. The air inlet velocity is set to 2 m/s, the air inlet temperature is 278 K, and the external environment is 274 K. The temperature field changes of the obtained air flow channel and heat absorb plate are shown in Figure 4.



(a) Temperature field of the air flow channel.



(b) Temperature field of the heat absorb plate.

Figure 4. Temperature field of two types of SAHs with heat absorb plate structures.

The different temperature color scales in Figure 4 are adopted to better illustrate the temperature difference between the sinusoidal-corrugated SAH and triangular-corrugated SAH. Figure 4(a) shows the temperature field inside the air flow channel (left: sinusoidal corrugated plate, right: triangular corrugated plate). From the temperature field in Figure 4(a), the internal temperature dead zone of the air flow channel in the sinusoidal corrugated plate is relatively small, and the outlet temperature is relatively high. This situation indicates that the heat gain of air on the sinusoidal corrugated plate is relatively high, and the heat transfer process between the sinusoidal corrugated heat absorbing plate and the air is more complete. The sinusoidal corrugated plate can effectively destroy the thermal boundary layer and induce secondary flow, increasing the heat gain of air.

Figure 4(b) reflects the temperature field of the heat absorb plate (left: sinusoidal corrugated plate, right: triangular corrugated plate). From the temperature field in Figure 4(b), the high-temperature area of the sinusoidal corrugated plate is smaller, and the temperature area distribution is more distinct than that of the triangular corrugated plate. This situation indicates that the turbulence effect of air on the

sinusoidal corrugated plate is strong, the air flow range is wide, the heat transfer process between air and heat absorb plate is sufficient, and the heat transferred from the heat absorb plate to the air is relatively high. The average temperatures of the absorb plate for the sinusoidal-corrugated SAH and triangular-corrugated SAH are 417.9 K and 455.1 K, respectively.

The heat collection efficiency η of SAH is the important criterion for evaluating SAH's heat collection performance. The heat collection efficiency η is the ratio of the energy obtained by the heated air to the amount of solar radiation irradiated onto the surface of SAH. The calculation formula for η is as follows:

$$\eta = \frac{cm(T_0 - T_i)}{A_c G_T} \tag{9}$$

c is specific heat capacity, kJ/kg·K; m is mass flow rate of air, kg/s; T_0 is air outlet temperature, K; Ti is air inlet temperature, K; A_c is SAH heat collection area, m^2; and G_T is solar radiation intensity, W/m^2.

During the heat transfer process, the heat of SAH will dissipate into the external environment, mainly including top heat loss U_t, bottom heat loss U_b, and edge heat loss U_e. The top heat loss coefficient U_t in the study is calculated using the empirical formula proposed by Klein [36]. The calculation formula for the bottom heat loss coefficient U_b is as follows:

$$U_b = \frac{k}{d} \tag{10}$$

k is thermal conductivity of bottom insulation material; and W/m·K, d is thickness of bottom insulation material, m.

The calculation formula for the edge heat loss coefficient U_e is as follows:

$$U_e = \frac{kA_e}{dA_c} \tag{11}$$

A_e is side area of SAH, m^2.

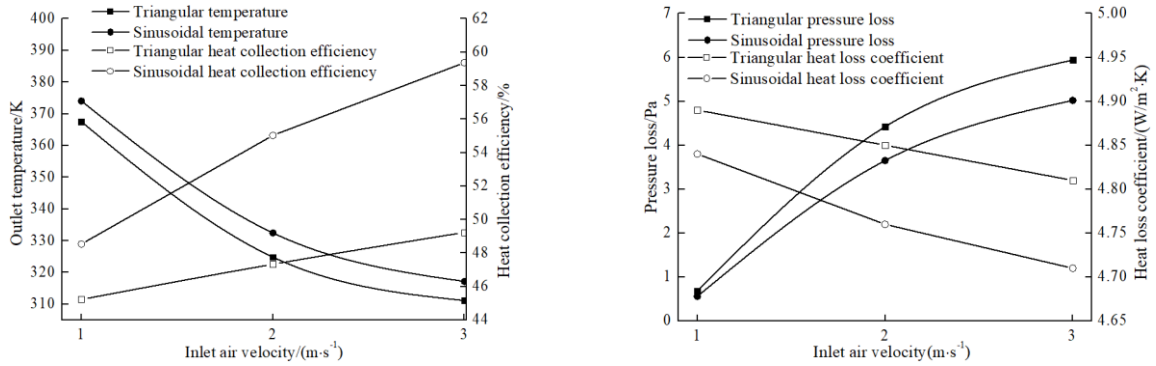
The total heat loss coefficient U_L of SAH is as follows:

$$U_L = U_t + U_b + U_e \tag{12}$$

The calculated curve data is obtained by adjusting the air inlet velocity to 1 m/s and 3 m/s, while controlling all other boundary conditions remains constant, as shown in Figure 5.

Figure 5 indicates the various data of two types of corrugated heat absorb plate SAHs at different air flow velocities. Figure 5(a) shows the relationship between air outlet temperature and heat collection efficiency. From the curve changes in Figure 5(a), as the air inlet velocity increases, outlet temperature gradually decreases, while the heat collection efficiency of SAH gradually increases. This is because when the air inlet flow rate is low, the air inlet flow rate per unit time is small, and the contact time between the air and the heat absorb plate is long, so the outlet temperature of the air is higher. When the air inlet flow rate is high, the air inlet flow rate per unit time is large, the contact time between the air and the heat absorb plate is short, and the heat exchange time is short, so the air outlet temperature is lower. Due to the increase in air flow rate being higher than the change in temperature,

it can be calculated from formula (7) that the heat collection efficiency of SAH increases. The decrease in air outlet temperature and the increase in heat collection efficiency slowly, indicating that when the air inlet flow rate reaches the certain stage, the impact on air outlet temperature and SAH heat collection efficiency is minimal.



(a) Outlet temperature and heat collection efficiency. (b) Pressure loss and heat loss coefficient.

Figure 5. Calculation data curve of two types of corrugated plate SAHs.

By comparing the two types of corrugated plate SAH, the air outlet temperature and heat collection efficiency of the sinusoidal corrugated plate SAH are higher. This indicates that the turbulence intensity of the air on the sinusoidal corrugated plate is greater, and the heat exchange between the sinusoidal corrugated plate and the heat absorb plate is greater. The overall heat transferred to the air by the sinusoidal corrugated plate is also greater. After comparison, the highest outlet temperature of the air is 374.05 K, and the maximum heat collection efficiency is about 59.37% (inlet air velocity 3 m/s). Compared to the maximum heat collection efficiency of 57.34% in reference [1], there is an improvement.

Figure 5(b) reflects pressure loss and heat dissipation coefficient variation of two types corrugated SAH with respect to air inlet velocity. From the curve change in Figure 5(b), the pressure loss in air channel increases with the increase of air flow velocity, while the heat dissipation coefficient shows a decrease. Because the air inlet velocity increases, the turbulence effect of the air on the heat absorb plate is enhanced, and the pressure inside the flow channel increases. The increase in air flow increases the amount of heat absorbed by the air on the heat absorb plate, resulting in a decrease in the external heat dissipation of SAH, thus reducing the overall heat dissipation coefficient of SAH.

By comparing the data curves of two types corrugated SAH, the pressure loss and heat dissipation coefficient of sinusoidal corrugated SAH are lower than those of the triangular corrugated plate. This result indicates that the flow state of air on the sinusoidal corrugated plate is better than that on the triangular corrugated plate, and the pressure loss is smaller. Additionally, the heat transfer efficiency is higher compared to the sinusoidal corrugated plate, so the heat dissipation coefficient is smaller. After calculation, the minimum pressure loss is about 0.56 Pa, and the minimum heat dissipation coefficient is about 4.71 W/m·K. Compared to the minimum pressure loss of 4.32 Pa in reference [37], the pressure loss has been significantly reduced.

The thermal-hydraulic performance of the two SAH configurations is evaluated by comparing the PEC, which is defined as:

$$\mathrm{PEC} = \frac{Nu / Nu_0}{(f / f_0)^{1/3}} \tag{13}$$

$$Nu = \frac{h \cdot D_h}{\lambda}, Nu_0 = \frac{h_0 \cdot D_h}{\lambda} \tag{14}$$

$$h = \frac{q_w}{T_w - T_b}, h_0 = \frac{q_{w0}}{T_{w0} - T_{b0}} \tag{15}$$

$$D_h = \frac{4A_c}{P_w} \tag{16}$$

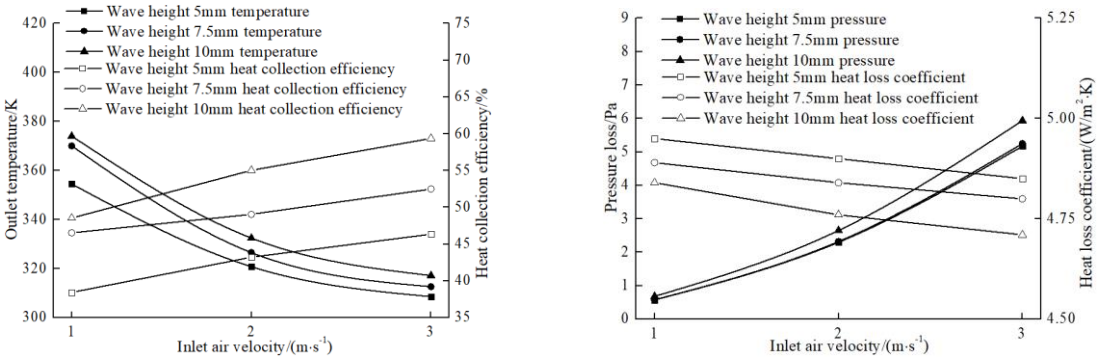
$$f = \frac{\Delta P \cdot D_h}{2 \cdot \rho \cdot u_a{}^2 \cdot L} \tag{17}$$

Nu is the Nusselt number; Nu_0 is the Nusselt number of the smooth flat plate; f is the friction factor; f_0 is the friction factor of smooth flat plate; h is the convective heat transfer coefficient, W/m^2·K. D_h is the hydraulic diameter, m; h_0 is the convective heat transfer coefficient of smooth flat plate, W/m^2·K; q_w is the heat flux, W/m·K; T_w is the average temperature of heat absorb plate, K; T_b is the average temperature of passage, K; q_{w0} is the heat flux of the smooth flat plate, W/m·K; T_{w0} is the average temperature of the smooth flat heat absorb plate, K; T_{b0} is the average temperature of the smooth flat plate passage, K; P_w is he wetted perimeter, m; $\triangle P$ is the pressure loss, Pa; u_a is the average velocity in passage, m/s; and L is the heater length, m.

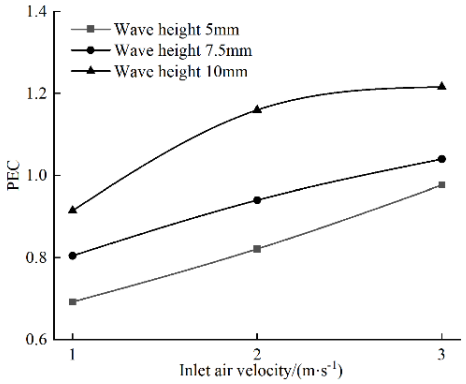
The calculation results from Eqs (12)–(16) show that PEC of the triangular-corrugated SAH is approximately 1.09, while that of the sinusoidal-corrugated SAH is about 1.14. Based on the comprehensive analysis of thermal efficiency, pressure loss, heat loss coefficient, and PEC, the sinusoidal-corrugated SAH exhibits superior thermal performance compared with the triangular-corrugated SAH within inlet air velocity range of 1–3 m/s.

3.2. Analysis and comparison of different wave heights

After comparing the heat collection performance of two types of corrugated plate SAH in Section 3.1, it can be concluded that compared to the triangular corrugated plate SAH, sinusoidal corrugated plate SAH not only has higher outlet temperature and heat collection efficiency, but also has a lower pressure loss and heat dissipation coefficient. In the research of sinusoidal corrugated plate SAH's heat collection performance, the high sinusoidal is the important factor affecting the SAH's heat collection performance. The wave height size will affect the pressure loss inside the flow channel, the heat gain of air, and the overall heat dissipation of SAH. On the basis of a wave height of 10 mm, adjust the wave height to 5 mm and 7.5 mm, and the calculated results are shown in Figure 6.



(a) Outlet temperature and heat collection efficiency. (b) Pressure loss and heat loss coefficient.



(c) PEC.

Figure 6. Calculation data curve of different wave heights (5 mm, 7.5 mm, and 10 mm).

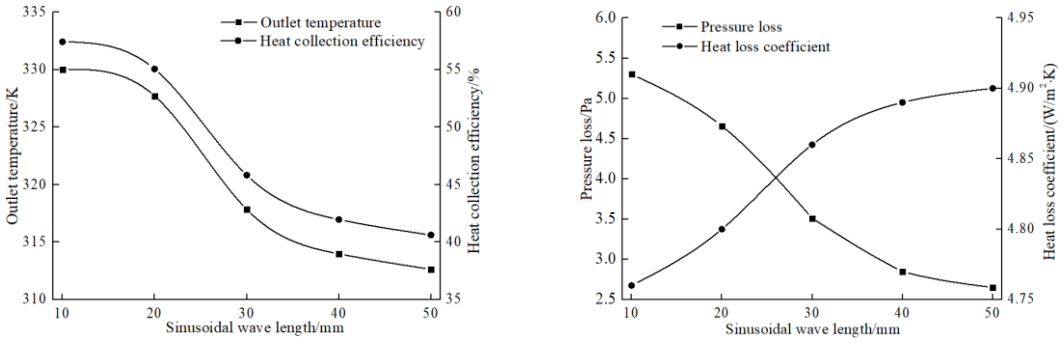
Figure 6 reflects the heat collection performance parameter curves of SAH with different wave heights under the condition of wavelength 10 mm. Figure 6(a) reflects the relationship between the air outlet temperature and heat collection efficiency. From the curve changes in Figure 6(a), the air outlet temperature decreases with the air inlet velocity increase, and the heat collection efficiency of SAH increases, but the rate of increase gradually slows. Comparing different wave heights, at the same air flow velocity, the higher the wave height, the higher the outlet temperature and heat collection efficiency. This is because when the wave length is fixed, the increase in wave height enhances the turbulence between the air and the heat absorb plate, increases the air internal turbulence intensity, strengthens the heat transfer between the air and the heat absorb plate, and increases the heat gain. Therefore, the air outlet temperature and the SAH heat collection efficiency are improved.

Figure 6(b) reflects the pressure loss and heat dissipation coefficient. From the curve changes in Figure 6(b), the pressure loss inside the SAH channel increases with the air flow velocity increase, while the heat dissipation coefficient decreases accordingly. Comparing the pressure loss and heat dissipation coefficient of different wave heights, we find that at the same air inlet velocity, the higher the wave height value, the greater the pressure loss, and the difference in pressure loss gradually increases with the air inlet velocity increase; as the wave height increases, the air flow channel narrows and the turbulence inside the air increases, resulting in the difference in pressure loss increase. Additionally, the heat dissipation coefficient of SAH gradually decreases because as the wave height increases, the heat transfer between the air and the heat absorbing plate is significantly enhanced,

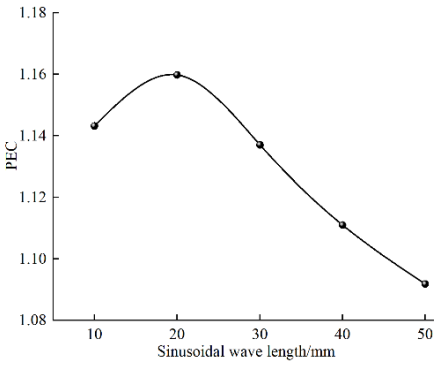
resulting in an increase in the amount of heat obtained and the decrease in the external heat dissipation of SAH. Therefore, the heat dissipation coefficient of SAH decreases. After calculation, when the wave height is 10 mm, the highest outlet temperature is 374.05 K, and the highest heat collection efficiency is 59.37%. Figure 6(c) shows PEC under different wave height and inlet velocity conditions. As indicated by the curves in the figure, an increase in wavelength and inlet velocity does cause the PEC to increase, but the rate of increase gradually slows.

3.3. Analysis and comparison of different wavelengths

In the research of sinusoidal corrugated plate SAH's heat collection performance parameters, the sinusoidal wavelength is also the significant factor affecting the SAH's heat collection performance. Smaller wavelengths will enhance the disturbance intensity of air on the heat absorb plate, increase the turbulence inside the air, while smaller wavelengths will increase the pressure inside the flow channel. Thus, we adjust the wavelength to 10–50 mm, calculate the heat collection parameters of SAH under the conditions of wave height 10 mm, set air inlet velocity as 2 m/s, the air temperature to 278 K, and ambient temperature to 274 K. The calculated results are shown in Figure 7.



(a) Outlet temperature and heat collection efficiency. (b) Pressure loss and heat loss coefficient.



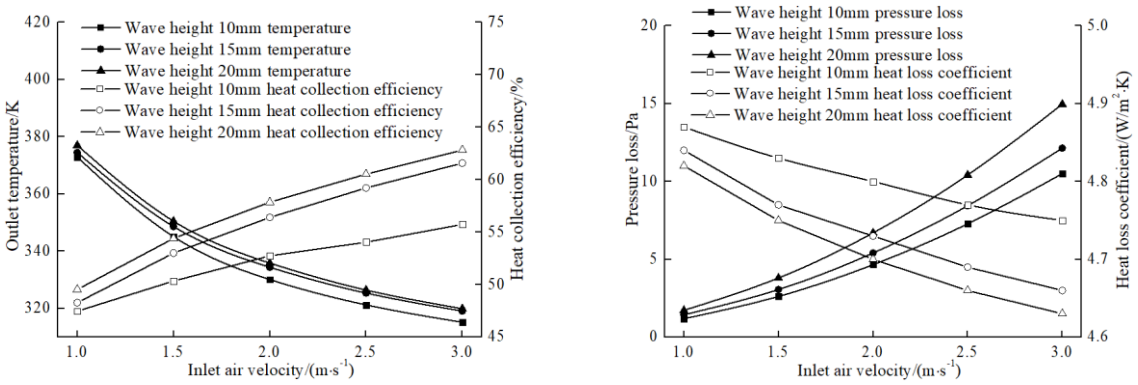
(c) PEC of different SAH wavelengths.

Figure 7. Calculation data curve of different SAH wavelengths.

Figure 7 reflects the calculation curves of heat collection parameters for different wavelengths. Figure 7(a) indicates the relationship between the air outlet temperature of sinusoidal corrugated plate

SAH and the SAH heat collection efficiency. From the curve in Figure 7(a), the outlet temperature of air and the heat collection efficiency decrease with sinusoidal wavelength increase. When the sinusoidal wavelength is at a smaller value, the turbulence effect of air on the sinusoidal corrugated plate is stronger, and the heat transfer between air and the heat absorb plate is stronger. The air obtains more heat on the heat absorb plate, so the air outlet temperature and the SAH heat collection efficiency are higher. As the wavelength increases, the decrease in air outlet temperature and SAH heat collection efficiency gradually decreases. This is because when the wavelength increases to the certain stage, the sinusoidal corrugated plate is very close to a flat plate, and the wavelength has little effect on the air outlet temperature and heat collection efficiency.

Figure 7(b) indicates the pressure loss and heat dissipation coefficient variation curve inside the SAH channel. From the curve variation in Figure 7(b), the pressure loss inside the air flow channel decreases with the wavelength increase. This is because when the sinusoidal wavelength is at a smaller value, the turbulent effect between the air and heat absorb plate is stronger, and the turbulent fluctuations inside the air are severe and obvious, resulting in larger pressure loss in the flow channel. As the wavelength value increases, the turbulence effect of air decreases, and the internal pressure decreases, resulting in a decrease in pressure loss. The heat dissipation coefficient increases with the wavelength increase, because when the sinusoidal wavelength is smaller, the heat transfer process between the air and the heat absorb plate is stronger, and more heat is absorbed, so the external heat dissipation of SAH is lower, and the heat dissipation coefficient is smaller. The amplitude of pressure loss and heat dissipation coefficient decrease with the sinusoidal wavelength increase. This indicates that when the sinusoidal wavelength increases to the certain stage, the wavelength has little effect on the pressure loss and heat dissipation coefficient of SAH. After calculation, it is known that there is the turning point in the air outlet temperature and heat collection efficiency when the wavelength is 20 mm, and the heat collection efficiency at this time is smaller compared to the 10 mm wavelength (55.03%) at 52.73%. The pressure loss is 4.66 Pa, and the heat dissipation coefficient is 4.8 W/m·K. Figure 7(c) shows the PEC at different wavelengths. The PEC calculation data indicate that the PEC is highest at a wavelength of 20 mm and then decreases. Therefore, compared to other wavelength conditions, the thermal performance is optimal at 20 mm.



(a) Outlet temperature and heat collection efficiency. (b) Pressure loss and heat loss coefficient.

Figure 8. Calculation data curve of different wave height under different wavelength (10 mm, 15 mm, and 20 mm).

In the research of heat collection parameters at wavelength 10 mm, the air outlet temperature, SAH heat collection efficiency, and heat dissipation coefficient at wave height 7.5 mm are not significantly different from those at wave height 10 mm, and pressure loss is smaller. Thus, the most suitable wave height size can be studied in the sinusoidal ripple SAH with wavelength 20 mm. Thus, we adjust the sinusoidal wave height to 10, 15, and 20 mm, and perform simulation calculations while ensuring that the air inlet temperature and ambient temperature remain unchanged. The results obtained are shown in Figure 8.

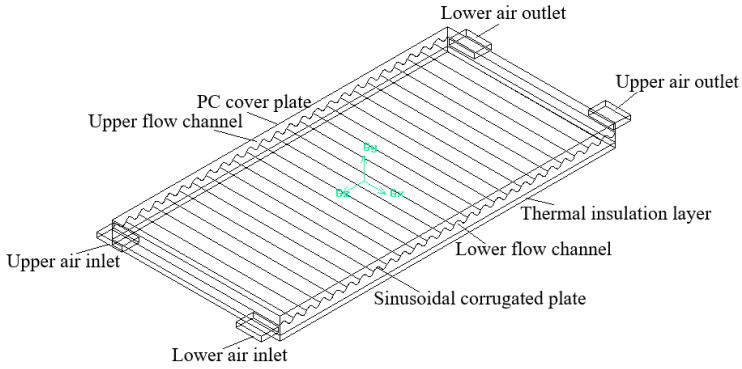
Figure 8 shows the variation curves of SAH heat collection parameters with different wave heights and sizes at wavelength 20 mm as the function of air inlet velocity. Figure 8(a) indicates the relationship between the SAH air outlet temperature and heat collection efficiency. According to the data in Figure 8, outlet temperature and heat collection efficiency at wave height 15 mm are not significantly different from those at wave height 20 mm. This indicates that when the wave height exceeds 15 mm, the sinusoidal wave height has little effect on the heat gain of air inside the SAH. Figure 8(b) shows the pressure loss and heat dissipation coefficient inside the SAH air channel. Moreover, when air inlet velocity is lower, the difference between pressure loss and heat dissipation coefficient is much smaller. After increasing the inlet velocity, the difference gradually becomes apparent, but the parameter difference between wave heights 15 mm and 20 mm is very small. According to the calculated data, when the wave height is 15 mm, the maximum heat collection efficiency is 61.58% (inlet air velocity 3 m/s), the maximum pressure loss is about 12.14 Pa, and the minimum heat dissipation coefficient is 4.66 W/m·K.

3.4. Double layer sinusoidal corrugated plate SAH

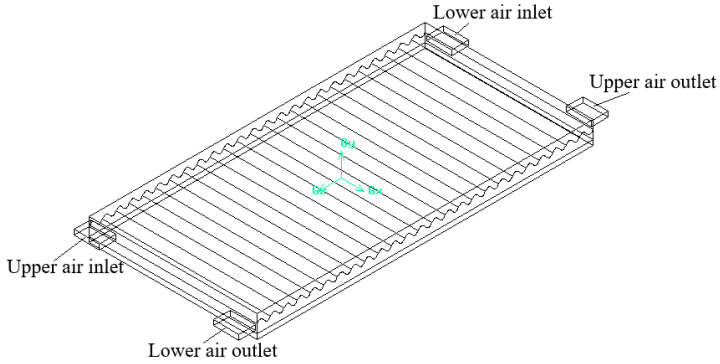
From the above research, the heat collection parameters and performance of a sinusoidal corrugated plate SAH with wavelength 20 mm and wave height 15 mm is better. Thus, the heat collection performance parameters of a double-layer sinusoidal corrugated plate SAH will be studied and analyzed. As such, the air inlet mode of double-layer SAH is divided into parallel and reverse flow. The double-layer SAH model is established under the condition of ensuring a wavelength of 20 mm and wave height 15 mm, and the SAH structure dimensions are unchanged. The specific model is shown in Figure 9.

Figure 9 reflects the physical model of the double-layer corrugated plate SAH. Figure 9(a) indicates the air flow forward mode, and Figure 9(b) shows the air flow backward mode. Under conditions where solar radiation, air inlet flow velocity, SAH collector area, and channel height are the same as those of single-layer duct SAH, simulation calculations are performed for the SAH systems with the two different air intake methods. The results are shown in Figure 10.

Figure 10 illustrates the thermal performance curves of the double-layer sinusoidal corrugated plate SAH under two distinct air inlet configurations. Figure 10(a) presents the outlet air temperatures for the upper and lower air channels under each configuration. Analysis of the data reveals that the difference in outlet temperature between parallel-flow and reverse-flow configurations is minimal for the upper channel, and the overall outlet temperatures of upper channel are lower than those of lower channel. This is primarily because the upper channel is directly exposed to solar radiation and experiences convective heat exchange with the PC cover plate, resulting in greater overall heat loss compared to the lower channel.

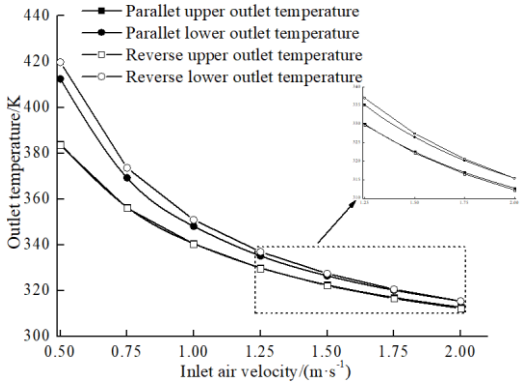


(a) Parallel flow method.

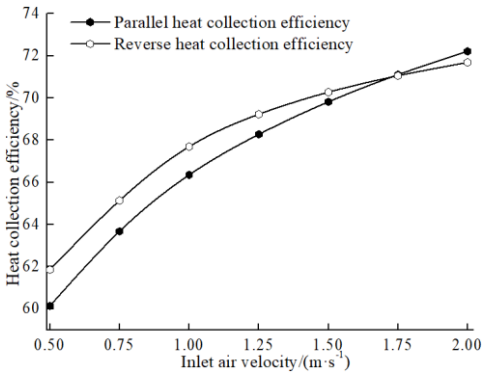


(b) Reverse flow method.

Figure 9. Double layers sinusoidal corrugated plate SAH model.



(a) Outlet temperature.



(b) Heat collection efficiency.

Figure 10. Collection parameters for two import methods.

For the lower channel, the disparity in outlet temperature between both the flow configurations diminishes progressively as inlet air velocity increases. This trend can be attributed to the residence time of air within the channel. At lower air velocities, the extended residence time enables the air to approach thermal equilibrium with the heated sinusoidal corrugated plate, enabling the reverse-flow arrangement to extract the greater amount of heat compared to the parallel-flow arrangement.

Conversely, at the higher air velocities, the shortened residence time limits the duration available for effective heat exchange. Under such conditions, air temperature rise becomes predominantly governed by the short-term heat transfer intensity. In this regime, the counter-flow configuration exhibits the reduced heat gain per unit air mass flow rate, consequently leading to the more pronounced decline in outlet temperature relative to the parallel-flow configuration.

Figure 10(b) presents the thermal efficiency of the SAH under the two air inlet configurations. As indicated by the curves, at lower air velocities, the reverse-flow configuration exhibits superior collection efficiency compared to the parallel-flow arrangement. However, this performance gap diminishes progressively with increasing airflow rates. This behavior can be attributed to the following mechanisms: Under low-velocity conditions, the counter-flow configuration benefits from recovering additional heat from the opposite side of the absorb plate, thereby enhancing the overall SAH efficiency through more complete heat exchange. As airflow rate increases, the amount of recoverable heat in the counter-flow mode gradually decreases, resulting in a lower rate of efficiency improvement compared to the parallel-flow mode. The pressure losses for the co-current configuration are 5.17 Pa and 5.66 Pa, respectively. The pressure losses for the counter-current configuration are 5.17 Pa and 5.06 Pa, respectively.

Based on the curve analysis, the maximum temperature difference between the two inlet configurations is calculated to be 7.32 K. When the inlet air velocity is 2 m/s, the heat collection efficiency in downstream mode reaches a peak of 72.22%. Compared to the maximum heat collection efficiency of 64.11% in reference [35], the heat collection efficiency has been improved by 8%. Furthermore, under the same flow rate conditions, the heat collection efficiency of double-layer duct SAH is at least 66%, which exceeds that of single-layer duct SAH (56%). Notably, when the inlet air velocity exceeds 1.75 m/s, the thermal efficiency of the parallel-flow configuration surpasses that of the reverse-flow arrangement. Furthermore, curve fitting is applied to the performance data of both configurations, with the results illustrated in Figure 11.

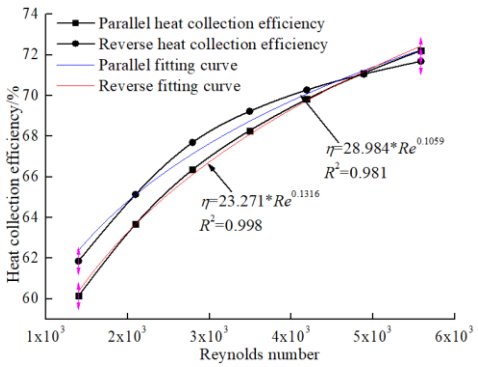


Figure 11. Fitting curve of two import methods of heat collection efficiency.

$$\mathrm{Re} = \frac{u_{in} \cdot D_h}{\mu} \tag{18}$$

u_{in} is inlet air velocity, m/s; and μ is dynamic viscosity, Pa·s.

Figure 11 presents the fitting curves of SAH thermal efficiency as the inlet air *Re* function. The number of fitting points corresponds to different air *Re* values (7), and the fitting method is nonlinear

fitting. As shown in Figure 11, the thermal efficiency increases with rising *Re*, though the rate of this increase gradually diminishes. The coefficients of determination (R^2) for the fitting curves of the two inlet configurations are 0.981 and 0.998, respectively, indicating that the fitting relationships provide the reliable prediction of the SAH thermal efficiency. The fitted correlations are applicable in an *Re* range of 1×10^3–6×10^3 at sinusoidal plate SAH.

4. Conclusions and prospects

4.1. Conclusions

To optimize the heat collection performance of SAH and improve the heat collection efficiency, this research starts from the sinusoidal corrugated plate SAH and uses simulation calculation methods to analyze the structural parameters that affect the heat collection performance of the sinusoidal corrugated plate SAH, including sinusoidal wavelength and wave height, and analyze the influence of the inlet method on the dual duct SAH. The conclusions drawn are as follows:

1. Compared to triangular corrugated plates, sinusoidal corrugated plate SAH has higher heat collection efficiency and a lower pressure loss and heat dissipation coefficient.
2. The higher the wave height of the sinusoidal corrugated plate, the greater the heat collection efficiency and pressure loss of SAH, but the smaller the heat dissipation coefficient. The maximum heat collection efficiency is 59.37%, and the minimum heat dissipation coefficient is 4.71 W/m^2·K.
3. The larger the wavelength of the sine wave patterned plate, the lower the heat collection efficiency and pressure loss of SAH but the larger the heat dissipation coefficient. The optimal wave height/wavelength is 0.75. Heat collection efficiency is 61.58%, pressure loss is 12.14 Pa, and the heat dissipation coefficient is 4.66 W/m·K.
4. The inlet velocity of the dual duct SAH is less than 1.75 m/s, and the heat collection performance of the parallel mode is higher than that in reverse mode. Heat collection efficiency of SAH increases with inlet *Re* increase, but the increased magnitude gradually slows. The fitting curve coefficient of determination for the parallel and reverse SAH flow modes are 0.981 and 0.998, respectively. The fitted correlations are applicable in an *Re* range of 1×10^3–6×10^3.

4.2. Prospects

Based on the aforementioned research content, future research work is as follows:

1. Physical collectors will be manufactured, and indoor and outdoor comprehensive test platforms will be built to carry out performance experiments under multiple air velocity and solar irradiance conditions for numerical model calibration.
2. The range of corrugation geometric parameters will be expanded, and the thermal-hydraulic performance of various corrugation shapes will be compared.
3. The matching schemes of parallel and counter-flow double channels will be further optimized to improve the general design and calculation system of corrugated SAH. Furthermore, the experimental data included in the analysis will be used to validate the correlation equation.

Use of AI Tools Declaration

No generative artificial intelligence tools were utilized to generate text, figures or computational data in this manuscript. Grammarly was only used for English language polishing and grammar correction, and it does not participate in the formation of research ideas, result analysis and paper writing.

Acknowledgment

This work was supported by the Shandong Engineering Research Center of Low-Carbon Energy Internet of Things Technology (PT2025KJS004).

Conflict of interest statement

All authors declare that there are no conflicts of interest regarding the publication of this paper.

Author contributions

Liang Wang: Conceptualization, Methodology, Software, Formal analysis, Investigation, Supervision, Visualization, Resources, Funding acquisition, Writing—original draft, Writing—review & editing. Wenke Zhang: Investigation, Data Curation, Visualization. Xiaole Wang: Validation, Formal analysis. Binguang Jia: Validation, Writing—review & editing.

Reference

1. Wang L, Man Y (2018) Numerical simulation of baffled baffle plate solar air collector. *Renewable Energy Resour* 36: 997–1003. Available from: https://lib.cqvip.com/Qikan/Article/Detail?id=675669734.
2. Abdulla AN, Alomar OR (2026) Performance of solar air heater collector with jet impingement and V-corrugated absorber plate: A comprehensive investigation towards high-efficiency applications in sustainable buildings trends. *Sol Compass* 17: 100152. https://doi.org/10.1016/j.solcom.2025.100152
3. Er-retby H, Es-sakali N, Mghazli MO, et al. (2026) Occupant behavior impact on energy efficiency and comfort in naturally ventilated buildings across climates using adaptive comfort: Models to metrics. *Appl Therm Eng* 284: 129032. https://doi.org/10.1016/j.applthermaleng.2025.129032
4. El-Bialy E, Shabaan DH, El-Babary A, et al. (2025) Recent advances in solar air heaters embedded with artificial rib roughness: A comprehensive review. *Int Commun Heat Mass Transfer* 168: 109444. https://doi.org/10.1016/j.icheatmasstransfer.2025.109444
5. Chen JN, Yang XM, Cui J, et al. (2025) Performance optimization and entropy-TOPSIS evaluation of a thermochemical solar thermal power generation system based on packed bed reactor exothermic characteristics. *Energy Convers Manage* 336: 19891. https://doi.org/10.1016/j.enconman.2025.119891
6. Raheem A, Siddique W, Waheed K, et al. (2024) Heat transfer enhancement of impinging jet-corrugated solar air heaters. *J Sol Energy Eng* 146: 041007. https://doi.org/10.1115/1.4064503

7. Kong DH, Bi R, Li GD, et al. (2024) Influence of corrugated jet plates on internal heat transfer and flow dynamics of double-wall cooling: Experimental-numerical approach. *Appl Therm Eng* 257: 124391. https://doi.org/10.1016/j.applthermaleng.2024.124391
8. Abd HM, Abdulrazzaq NM, Soheel AH (2024) Solar air heater energy and exergy enhancement using a V-corrugated wire mesh absorber: An experimental Comparison. *Energy* 309: 133136. https://doi.org/10.1016/j.energy.2024.133136
9. Abdulmejeed AEA, Tuncer AD, Khanlari A, et al. (2024) Investigation of combined parallel and Triple-pass v-corrugated solar air heater: A numerical and experimental Study. *Process Saf Environ Prot* 185: 1385–1398. https://doi.org/10.1016/j.psep.2024.03.107
10. Arshad Ahmed KR, Ganesh Kumar P, Naveen Kumar JP, et al. (2025) Numerical investigation in a solar air heater with V-corrugated and sinusoidal type absorber Plate. *Numer Heat Transfer, Part A* 87: 1–19. https://doi.org/10.1080/10407782.2025.2539146.
11. Alqsair UF (2025) Numerical simulation and optimization of a Chevron-Type corrugated solar air heater. *Energies* 18: 1821. https://doi.org/10.3390/en18071821
12. Abdulla AA, Mohammed AA, HusseinEK (2025) Improvement of the performance of the double pass solar air heater by using various shapes of absorber plate: An experimental analysis. *J Adv Res Fluid Mech Therm Sci* 128: 59–68. https://doi.org/10.37934/arfmts.128.1.5968
13. Azad MS (2024) Effective efficiency analysis of artificially roughed solar air heater by diagonally chamfered cuboid array. *Heat Transf Res* 55: 27–46. https://doi.org/10.1615/HeatTransRes.2024052712
14. Singh R, Narayanan R (2025) Comprehensive review of thermal and thermohydraulic performance in solar air heaters with advanced artificial roughness geometries. *Energies* 18: 6157. https://doi.org/10.3390/en18236157
15. Kandula J, Gugulothu SK, Muthyala R, et al. (2025) Hybrid numerical evaluation of Thermo-hydraulic and exergetic behaviour in solar air heaters with advanced arc rib Architectures. *J Therm Anal Calorim* 150: 20887–20907. https://doi.org/10.1007/s10973-025-15035-5
16. Singh R, Bhagoria JL, Narayanan R (2025) Experimental analysis of thermo-hydraulic performance of quadratic duct with artificial roughness on a single broad heated surface of the absorber plate of solar air Heater. *Case Stud Therm Eng* 72: 106415. https://doi.org/10.1016/j.csite.2025.106415
17. Almeshaal M, Palaniappan M, Matheswaran MM (2024) Assessment and enhancement of thermal performance for ring roughened finned jet impingement solar air heater for Low-temperature Applications. *Energy* 307: 132632. https://doi.org/10.1016/j.energy.2024.132632
18. Khimsuriya Y, Patel DK, Patel V, et al. (2025) Performance assessment of rotating spiral-shaped baffles built-in solar air heater: 4E and sustainability analysis. *Case Stud Therm Eng* 72: 106345. https://doi.org/10.1016/j.csite.2025.106345
19. Mohammad SI, Owida HA, Vasudevan.A, et al. (2025) Experimental investigation of thermal performance of a solar air heater with perforated obstacles on an absorber plate. *Energy Explor Exploit* 43: 2665–2685. https://doi.org/10.1177/01445987251356531
20. Noureini SG, Azadani LN (2025) Thermal performance enhancement of a solar air heater with different roughness Layouts. *Case Stud Therm Eng* 74: 106776. https://doi.org/10.1016/j.csite.2025.106776

21. Rajkumar P, Melvin Jones J, Nirmal Raj L, et al. (2024) Enhancing solar air heater performance with quatrefoil artificial roughness: An adaptive neuro-fuzzy system approach. *E3S Web of Conferences* 477: 00088. https://doi.org/10.1051/e3sconf/202447700088
22. Prasad JS, Datta A, Mondal S (2024) Numerical analysis of a solar air heater with offset transverse ribs placed near the absorber Plate. *Renewable Energy* 227: 120608. https://doi.org/10.1016/j.renene.2024.120608
23. Kanjirakat A, Kamath AM, Khan SA, et al. (2025) Enhancement of thermal performance in rectangular solar air heater duct using tetrahedron-shaped turbulators. *Sci Rep* 15: 43972. https://doi.org/10.1038/s41598-025-27762-8
24. Vijayakumar R, Kumar RV, Madhu P (2024) Investigation on energy, economic, and environmental aspects of double-pass solar air heater. *Environ Sci Pollut Res* 31: 39406–39420. https://doi.org/10.1007/s11356-024-33786-w
25. Sharma SL, Debbarma A (2024) Experimental study of reverse flow solar air heater having perforation and delta wing on absorber plate. *Energy Technol* 12: 202301246. https://doi.org/10.1002/ente.202301246
26. Aboub HQ, Khalifa AHN, Hamad AJ (2024) Heat transfer augmentation of multiple pass solar air heater with a metal mesh assisted corrugated absorber plate. *AIP Conference Proceedings* 3203: 040009. https://doi.org/10.1063/5.0213309
27. Wang Y, Wang J, Ma J, et al. (2025) Multi-parameters optimization design of downward jet solar air collector with corrugated absorber plate Structure. *Int Commun Heat Mass Transfer* 165: 109026. https://doi.org/10.1016/j.icheatmasstransfer.2025.109026
28. Li G, Guo T, Ye L, et al. (2025) Numerical investigation of inclined sinusoidal-corrugated target plates for enhancing flow and heat transfer in jet-to-crossflow impingement system. *Energy* 340: 137830. https://doi.org/10.1016/j.energy.2025.137830
29. Avargani VM, Maarof HA, Zendehboudi S (2023) Multiphysics CFD modeling to assess performance of a perforated multi-plate indirect solar dryer with a V-corrugated absorber surface. *Appl Therm Eng* 227: 120387. https://doi.org/10.1016/j.applthermaleng.2023.120387
30. Avargani VM, Maarof HA, Zendehboudi S (2025) Enhancing thermal and exergetic performance of solar air heating systems with PCM-integrated finned obstacles. *Energy* 326: 136149. https://doi.org/10.1016/j.energy.2025.136149
31. Jia BG, Song ZY, Li X, et al. (2025) Enhancing thermal performance: The evolution and future of solar air heaters with baffles. *Case Stud Therm Eng* 75: 107163. https://doi.org/10.1016/j.csite.2025.107163
32. Wang L (2022) Research on the collect heat performance of new type collector. *Energy Source Part A* 44: 9412–9427. https://doi.org/10.1080/15567036.2021.1954729.
33. El-Fakharany MK, Abo-Samra AA, Abdelmaqsoud AM, et al. (2024) Enhanced performance assessment of an integrated evacuated tube and flat plate collector solar air heater with thermal storage material. *Appl Therm Eng* 243: 122653. https://doi.org/10.1016/j.applthermaleng.2024.122653
34. Song Z, Xue Y, Jia B, et al. (2023) Introduction of the rectangular hole plate in favor the performance of photovoltaic thermal solar air heaters with baffles. *Appl Therm Eng* 220: 119774. https://doi.org/10.1016/j.applthermaleng.2022.119774
35. Jia BG, Liu F, Wang D, et al. (2019) Optimization of flow path for the spoiler solar air collector. *Chem Ind Eng Prog* 38: 819–825. https://doi.org/10.16085/j.issn.1000-6613.2018-0790

36. Klein SA (1975) Calculation of flat-plate loss coefficients. *Sol Energy* 17: 79–80. https://doi.org/10.1016/0038-092X(75)90020-1
37. Huang XX, Wang L, Li X (2025) Research on thermal performance and pressure loss of a new perforated-folded baffle solar air collector. *Numer Heat Transfer Part A* 86: 976–995. https://doi.org/10.1080/10407782.2023.2276886



AIMS Press

© 2026 the Author(s), licensee AIMS Press. This is an open access article distributed under the terms of the Creative Commons Attribution License (https://creativecommons.org/licenses/by/4.0)